Research Paper

EERI EARTHQUAKE SPECTRA

A probabilistic seismic hazard model for Mainland China

Earthquake Spectra
1–29

DOI: 10.1177/8755293020910754
journals.sagepub.com/home/eqs
SAGE

Yufang Rong, M.EERI[1], Xiwei Xu[2], Jia Cheng[2], Guihua Chen[3], Harold Magistrale, M.EERI[1], and Zheng-Kang Shen[4]

Abstract

We construct a probabilistic seismic hazard model for mainland China by integrating historical earthquakes, active faults, and geodetic strain rates. We delineate large seismic source zones based on geologic and seismotectonic characteristics. For each source zone, a tapered Gutenberg–Richter (TGR) distribution is used to model the total seismic activity rates. The TGR *a*- and *b*-values are calculated using a new earthquake catalog, while corner magnitudes are constrained using the seismic moment rate inferred from a geodetic strain rate model. For hazard calculations, the total TGR distribution is split into two parts, with smaller ($M_W < 6.5$) earthquakes being distributed within the zone using a smoothed seismicity method, and larger earthquakes put both onto active faults, based on fault slip rates and dimensions, and into the zone as background seismicity. We select ground motion models by performing residual analysis using ground motion recordings. Site amplifications are considered based on a site condition map developed using geology as a proxy. The resulting seismic hazard is consistent with the fifth-generation national seismic hazard model for most major cities.

Keywords

Seismic hazard, China, probabilistic seismic hazard analysis, seismic sources, site condition, ground motion

Date received: 4 June 2019; accepted: 1 February 2020

[1]Research Division, FM Global, Norwood, MA, USA
[2]Institute of Crustal Dynamics, China Earthquake Administration, Beijing, China
[3]Institute of Geology, China Earthquake Administration, Beijing, China
[4]Department of Earth, Planetary, and Space Sciences, University of California—Los Angeles, Los Angeles, CA, USA

Corresponding author:
Yufang Rong, Research Division, FM Global, 1151 Boston-Providence Turnpike, Norwood, MA 02062, USA.
Email: Yufang.rong@fmglobal.com

Introduction

China is frequently shaken by strong earthquakes and has abundant written records of earthquakes spanning over 3000 years. In 2015, China released the fifth-generation national seismic ground motion parameter zonation map, which became the current national standard for the building code (General Administration of Quality Supervision, Inspection and Quarantine of the People's Republic of China, 2015). The fifth-generation map included a horizontal peak ground acceleration (PGA) map, a map illustrating characteristic period (the second corner period) of response spectra, and the provision for adjusting PGA and characteristic period with site classes using the methodology described in Gao (2015). However, the hazard calculations can be neither reproduced nor extended by others because the details of data (e.g. boundaries of source zones and seismic activity parameters for each source zone) and methodology (such as how the active fault data were used) on the seismic hazard modeling were not given. The objective of this study is to develop a new seismic hazard model for mainland China. Taiwan is not included here because a seismic hazard model for Taiwan was developed and released in 2015 (Wang et al., 2016).

Seismicity models and appropriate ground motion models (GMMs) are the main components for probabilistic seismic hazard modeling. Seismicity models generally describe the earthquake occurrence or frequency with respect to magnitudes and locations. Common methods for constructing them comprise smoothing past seismicity, and employing a characteristic earthquake model to estimate earthquake occurrence on active faults (e.g. Fujiwara et al., 2006; Petersen et al., 2015; Wang et al., 2016). However, a fault database is not likely to include every seismogenic fault, and catalogs of historical earthquakes (throughout this article, we use the term "historical earthquakes" for both instrumental and pre-instrumental earthquakes) are often not long enough to characterize the rate and distribution of large earthquakes. We address these drawbacks in the modeling process by including additional useful information, geodetic-based strain rates. The Collaboratory for the Study of Earthquake Predictability (CSEP) experiment demonstrated that using geodetic strain rate in earthquake activity rate modeling is promising (Schorlemmer et al., 2018). Tectonic moment rate provides an upper limit for the seismic moment rate budget. Under the reasonable assumption that the long-term average rate of elastic strain is negligible in comparison to the rate of permanent strains accumulated by frictional faulting, tectonic moment rates can be calculated from a strain rate model.

In this study, we employ a simple but practical method to build seismicity models. The method integrates historical earthquakes, active faults, and geodetic strain rates (Rong et al., 2017). In the sections below, we describe some of the datasets compiled for this work and the process of GMM selection. The method and process for constructing seismicity models are discussed in detail. Hazard maps for mainland China and hazard curves for several major cities are displayed, followed by a comparison of present result with the fifth-generation national seismic ground motion parameter zonation map, and a discussion of model limitations.

Data for constructing seismicity models

Seismotectonics of China

Mainland China is located on the southeastern Eurasia plate. The collision of the India plate with the Eurasia plate not only uplifted the Himalayas and Tibet Plateau, but also

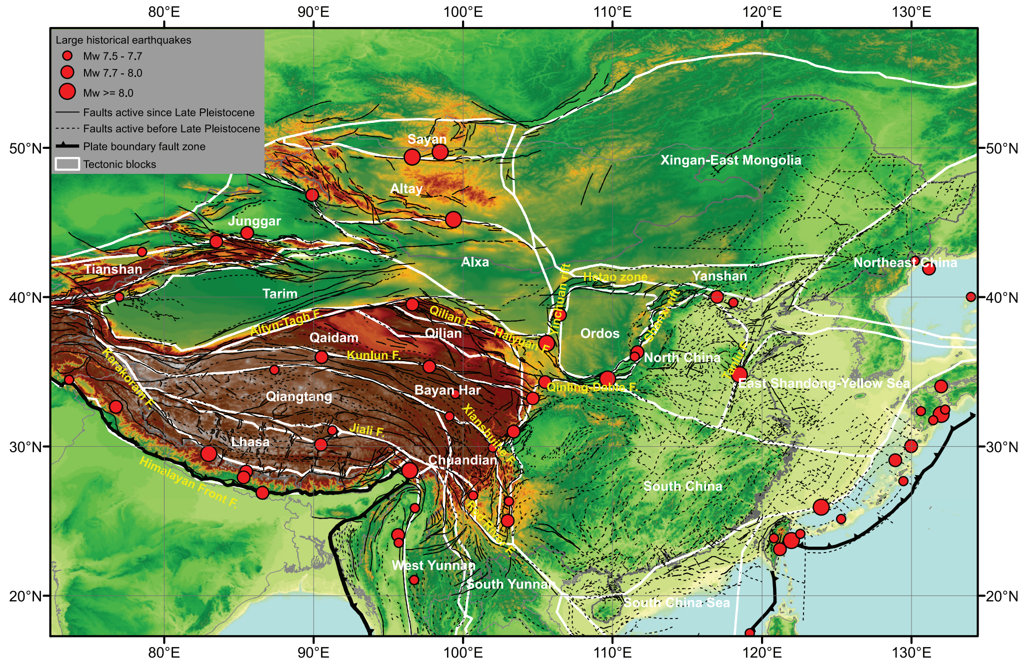

Figure 1. Tectonic blocks, faults, and large historical earthquakes in and around mainland China. The tectonic blocks, shown by white polygons, are modified from Zhang et al. (2003). Thin solid black lines indicate faults active since the Late Pleistocene, and thin dashed black lines indicate faults active before the Late Pleistocene. The fault data are from Xu et al. (2016). Large historical earthquakes ($M_W \geqslant 7.5$ from 780 BC to 2016) are shown by red dots.

deformed the Eurasian interior as far as 3000 km north of the Himalaya. The process of India-Eurasia collision and the eastward "escape tectonics" produced major active faults within and around the Tibet Plateau such as the Himalaya main thrust fault, Karakorum fault, Xianshuihe fault, Kunlun fault, Altyn-Tagh fault, Haiyuan fault, and Red River fault (Figure 1). These major faults zones cut the Tibetan Plateau into six active tectonic blocks: Lhasa, Qiangtang, Bayan Har, Qaidam, Qilian, and Chuandian (Figure 1) (Zhang et al., 2003). Recent large earthquakes in the region include the 2015 M_W 7.9 Gorkha, the 2008 M_W 7.9 Wenchuan, the 2001 M_W 7.8 Kokoxili, and the 1997 M_W 7.5 Manyi earthquakes.

North of the Tibet Plateau, the active Tianshan block is bounded by the relatively stable Tarim and Junggar blocks (Figure 1) (Zhang et al., 2003). The Tianshan block is composed of multiple near east-west striking thrust faults, and it accommodates a significant amount of north-south shortening. The Sayan, Altay, and Alxa blocks (Figure 1), located east of the Tarim and Junggar blocks, contain some of the largest strike-slip faults in the region. Three $M_W \sim 8$ earthquakes stuck the region in the last century.

Crustal deformation in eastern China is predominately along the rift zones around the Ordos block and the seismic zone in the Yanshan and North China blocks (Figure 1). Devastating earthquakes around the Ordos block include the 1920 $M_W \sim 8.3$ Haiyuan earthquake, 1556 $M_W \sim 8.0$ Shannxi and 1303 $M_W \sim 8.0$ Hongdong earthquakes. Great earthquakes around the North China block include the 1679 $M_W \sim 8.0$ Sanhe-Pinggu and

1976 M_W 7.6 Tangshan earthquakes. The Tanlu fault is the longest fault in eastern China and hosted the 1668 M_W 8.0–8.5 Tancheng earthquake (Figure 1). However, the slip rate along the fault is small. The South China, Xingan-East Mongolia, and Northeast blocks in eastern China are relatively stable and characterized by low seismic activity.

For the construction of seismicity models, we compile an M_W-based historical earthquake catalog and a seismogenic fault source database. We also use a high-resolution strain rate map developed from Global Positioning System (GPS) observations (Wang and Shen, 2020) in the modeling process.

An M_W-based historical earthquake catalog

China has an over 3000-year-long earthquake record, listed in various Chinese earthquake catalogs. The magnitudes in those catalogs were expressed in M_S. We select three M_S-based Chinese and two global M_W-based catalogs to develop M_S–M_W regression relationships for different time periods. The Chinese catalogs are as follows: Catalogue of Chinese Historical Strong Earthquakes that collected 1034 $M_S \geqslant 4.7$ earthquakes in China from 2300 BC to 1911 AD (Min et al., 1995), Catalogue of Chinese Present Earthquakes (Wang et al., 1999) with 4289 $M_S \geqslant 4.7$ earthquakes from 1912 to 1990, and the online catalog (http://www.csndmc.ac.cn) of the China Earthquake Networks Center (CENC) which reported more than 10,000 $M_S \geqslant 4.0$ instrumentally recorded earthquakes occurring in China and surrounding areas since 1970. The global catalogs are the ISC-GEM catalog (Storchak et al., 2013) which listed $M_W \geqslant 5.5$ events in the time period of 1900–2012, and the Global CMT catalog for the time period of 1976–2015 with M_W as small as 4.5.

We perform magnitude regressions using the general orthogonal regression method over two magnitude ranges ($5.5 \leqslant M_S < 7.0$ and $M_S \geqslant 7.0$) and over three time periods (1900–1965, 1966–1975, and 1976–2015). The three time periods are based on the times of major network upgrades in China. The middle period seems to be short. However, covariance analysis demonstrates that the regression relationships for 1966–1975 are significantly different from those for other time periods. Because the source parameters of large earthquakes ($M_S \geqslant 7.0$) are usually reviewed and modified by CENC, and as a result, the magnitudes are more accurate than those of small- and medium-sized earthquakes, we use bilinear regressions to accommodate potentially different regression slopes above and below M_S 7.0.

For the earthquakes from 1900 to 1965, the derived relationships are as follows:

$$\begin{aligned}&M_W = (1.06 \pm 0.08)\,M_S - (0.58 \pm 0.60) \quad \text{for } M_S \geqslant 7.0\\&\text{and}\\&M_W = (0.74 \pm 0.03)\,M_S + (1.64 \pm 0.17) \quad \text{for } M_S < 7.0\end{aligned} \tag{1}$$

For the time period of 1966–1975, the relationships are as follows:

$$\begin{aligned}&M_W = (1.05 \pm 0.27)\,M_S - (0.90 \pm 2.02) \quad \text{for } M_S \geqslant 7.0\\&\text{and}\\&M_W = (0.62 \pm 0.11)\,M_S + (2.13 \pm 0.69) \quad \text{for } M_S < 7.0\end{aligned} \tag{2}$$

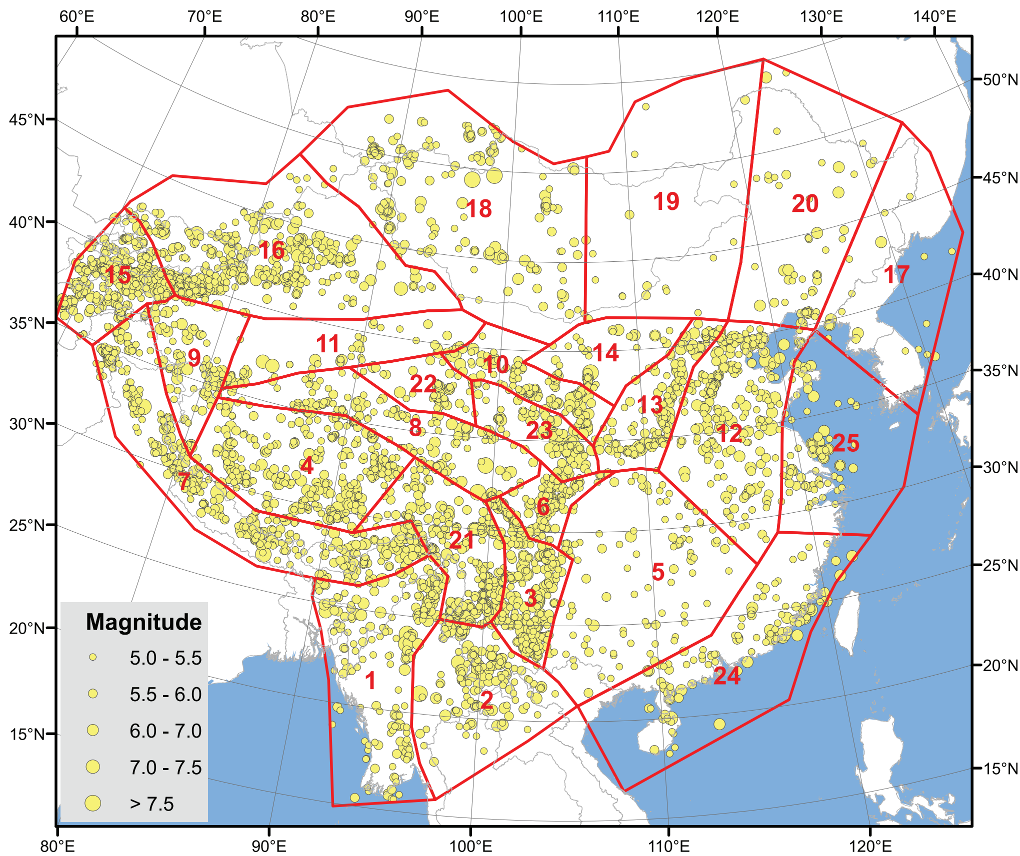

Figure 2. Shallow (hypocentral depth less than 35 km) $M_W \geqslant 5.0$ earthquakes (yellow dots, size scaled according to magnitude) in our M_W-based historical earthquake catalog. Red polygons are seismic source zones for the crustal layer with IDs labeled.

For the earthquakes from 1976 to 2015, the relationships are as follows:

$$M_W = (1.28 \pm 0.20)\, M_S - (2.42 \pm 1.47) \quad \text{for } M_S \geqslant 7.0$$
$$\text{and} \qquad (3)$$
$$M_W = (0.86 \pm 0.03)\, M_S + (0.59 \pm 0.18) \quad \text{for } M_S < 7.0$$

Using the regression relationships, we convert M_S in the Chinese catalogs to M_W and merge them with the M_W catalogs. We also find that some smaller earthquakes were recorded in the global catalogs and included in a recently compiled M_W-based global catalog (Weatherill et al., 2016), but not included in the Chinese catalogs. We add those earthquakes in our catalog. The final catalog has about 15,700 earthquakes of $M_W \geqslant 4.0$. Figure 2 illustrates the earthquakes of $M_W \geqslant 5.0$ included in our M_W-based earthquake catalog, as well as the seismic source zones that we use for constructing seismicity models. Most of earthquakes recorded before 1900 were in eastern China because the historical earthquake record in eastern China is much longer than in western China. Further details of the catalog compilation can be found in Cheng et al. (2017).

Active faults and seismogenic fault sources

Geological faults are present in most areas of China. The most complete compilation of mapped and inferred active faults contains more than 6000 fault traces (Figure 1) (Xu et al., 2016). However, that database does not contain all the parameters, such as slip rate, dip, and rake, for every fault trace that are needed for seismic hazard modeling.

We consider only faults known to be active since the Late Pleistocene (thin solid black lines in Figure 1). We follow the guidelines provided by the Global Earthquake Model Faulted Earth working group (Litchfield et al., 2013) to convert active fault traces to seismogenic sources. We first simplify the fault traces by combining faults that are spatially close (parallel, or end-to-end). Then we go through the literature to collect parameters for as many faults as possible. This process results in about 550 seismogenic fault sources. Fault types are available for most of the faults, and for about 50% of them, slip rates are collected from the literature. For the faults whose dip angles are not available, 90° is assumed for strike-slip faults and 50° for other fault types.

GPS velocity data have been inverted for fault slip rates in most active tectonic regions of the world that have geodetic observations. We adopt the method that was used in the Sichuan-Yunnan region of China (Wang et al., 2008, 2015) and California (Zeng and Shen, 2016, 2014) to invert slip rates for the faults in mainland China (Rong et al., 2018). In this method, crustal deformation is assumed to be the result of slip on a network of linked faults, computed using a dislocation model in an elastic media (Okada, 1992). In the inversion process, fault slip across adjacent segments is connected, and the degree of slip continuity across fault junctions is optimally determined through evaluation of a trade-off between the data postfit residual and model resolution.

For mainland China, GPS data from the Crustal Movement Observation Network of China are processed (Wang and Shen, 2020). We inspect the velocities for spatial coherency and discard those having large uncertainties or apparent effects from the postseismic deformation of the 2008 Wenchuan and 2011 Tohoku earthquakes. We also obtain GPS velocity solutions for Mongolia (Calais et al., 2003), central and western Tien Shan (Zubovich et al., 2010), Pamir-Hindu Kush (Ischuk et al., 2013; Mohadjer et al., 2010), Kashmir (Schiffman et al., 2013), Northern Pakistan (Jouanne et al., 2014), Shillong Plateau of India (Vernant et al., 2014), India (Banerjee et al., 2008), Indo-Burman Plate Boundary (Gahalaut et al., 2013), Myanmar (Devachandra et al., 2014), South Korea (Jin and Park, 2006), and Taiwan (Hsu et al., 2009). Then we rotate these GPS solutions to the same reference frame, screen them for spatial coherency, and merge them with the data in mainland China. The merged GPS dataset after screening contains solutions at 2128 sites (Figure 3).

We create a network of linked faults with about 280 fault segments (Figure 4). Here, we use the term "fault segment" to refer to a fault section that can be represented using one set of strike, rake, dip, and slip rate; we do not mean that it will be ruptured by a single earthquake. In this network, some segments represent the motion of more than one fault because the GPS stations are not dense enough in western China and the velocity gradients are not large enough in eastern China for inverting slip rates on more fault segments. Since the fault-network modeling uses only slip on faults to simulate crustal motion, some of the boundary faults are extended to the far field (about 2000 km along strike) to accommodate the effect of relative motions of the boundary blocks. These fault extensions are northwest extension of the Tala fault (segment 272 in Figure 4), southwest extension of the Darvaz fault (segment 273 in Figure 4), south extension of the megathrust along the Andaman-Sumatra trench (segment 274 in Figure 4), south extension of the Saigang fault (segment

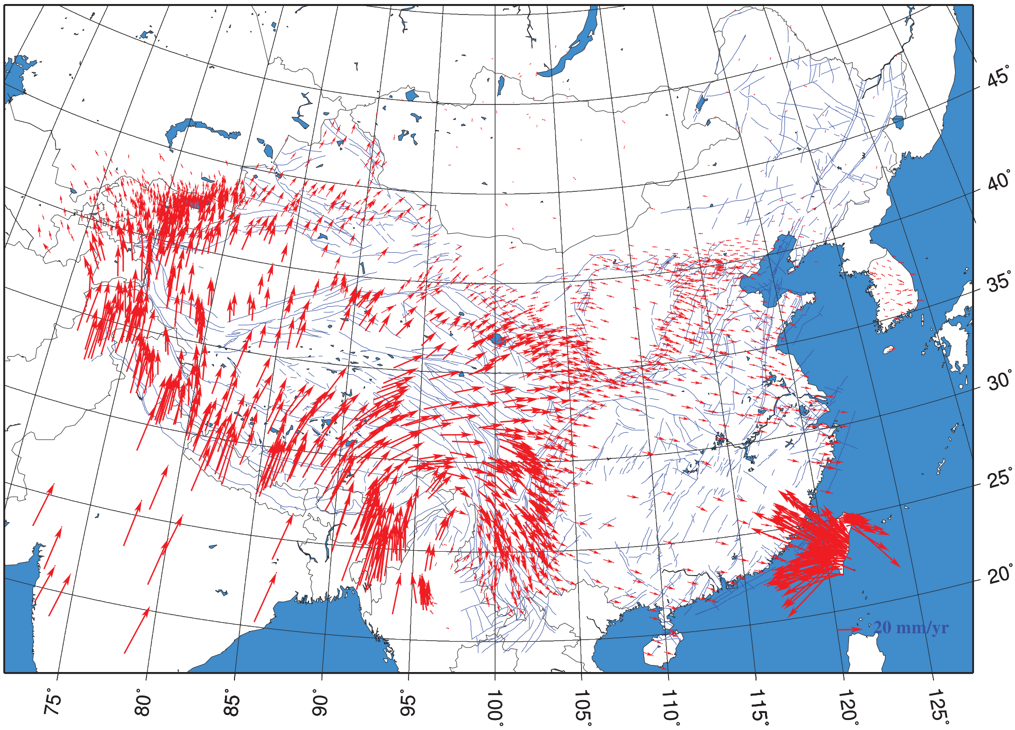

Figure 3. GPS velocity field (red arrows) with respect to stable Eurasia. Faults within China indicated by blue lines.

275 in Figure 4), northeast extension Yichun-Yitong fault (segment 276 in Figure 4), and north extension of the northern Lake Baikal fault (segment 277 in Figure 4). The computer code used in the studies by Wang et al. (2008), Wang et al. (2015), Zeng and Shen (2014), and Zeng and Shen (2016) employed the flat-Earth model, which was fine since the studies inverted fault slip rates at a regional scale. Because our study deals with a much larger geographic region, we modify the code to avoid geometric distortion due to the flat-Earth assumption. The slip rates collected from the literature are used as constraints in the inversion. The inverted slip rates are expressed by dextral or sinistral slip along fault parallel directions (Figure 5a) and convergence or divergence along fault normal directions (Figure 5b). The data fit is good overall. The only region which shows systematic and large postfit residuals is the Himalaya-India region, with the velocity residuals mainly in the fault normal direction. This is probably a result of the limitation of our model, which approximates deformation across a thrust fault as contraction across a vertical fault.

Finally, we combine the inverted slip rates with those collected from the literature. For the ~50% of the faults with slip rates available in the literature, we use those slip rates. For other faults, we use the inverted slip rates. Because the network of linked faults includes 280 fault segments whereas we have kept 550 fault sources for hazard modeling, the modeled slip rate on one linked-fault segment may represent the total slip rate of multiple faults. We therefore distribute the difference between inverted and collected slip rate onto the faults whose slip rates are unavailable from the literature using fault

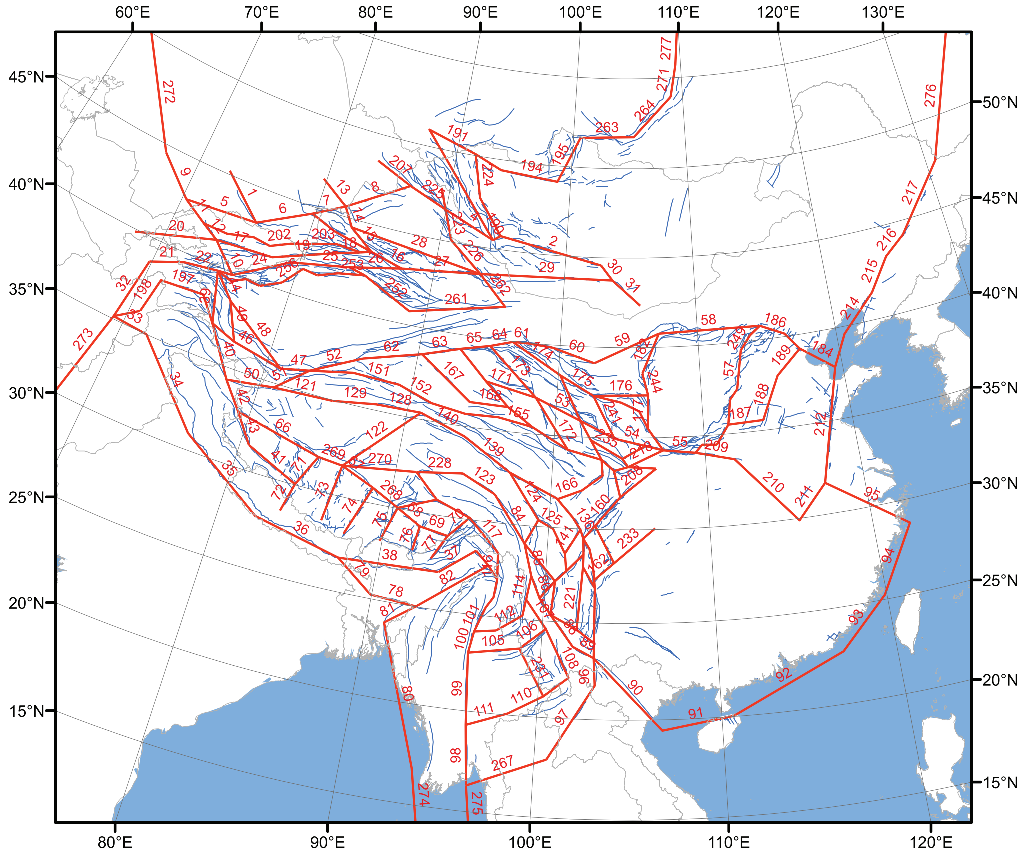

Figure 4. A network of linked faults (red lines, segments labeled by numbers). Note the faults are augmented with the addition of six segments (segments 272–277) extending to the far field to accommodate the effects of boundary block motions during data fitting. The light blue lines are traces of active faults.

geomorphologic expression as guidance of the fault activity. The final slip rates of the fault sources are displayed in Figure 6.

Earthquake source zonation and seismicity modeling

Methodology

Many traditional probabilistic seismic hazard analysis (PSHA) models are based on small seismic source zones, and the seismicity rate is assumed to be uniform within each of the source zones. However, small source zones often do not have sufficient records of historical earthquakes to robustly characterize the earthquake magnitude–frequency distribution. In our method, the modeled seismicity does not need to be uniformly distributed within each of the large seismic source zones. Instead, we assign the earthquake occurrence both to the background using a smoothed seismicity approach based on the location, size, and frequency of historical earthquakes, and onto the active faults based on the fault characteristics. Thus, we use large seismic source zones, and each zone represents a regional tectonic province with similar geologic and seismotectonic characteristics.

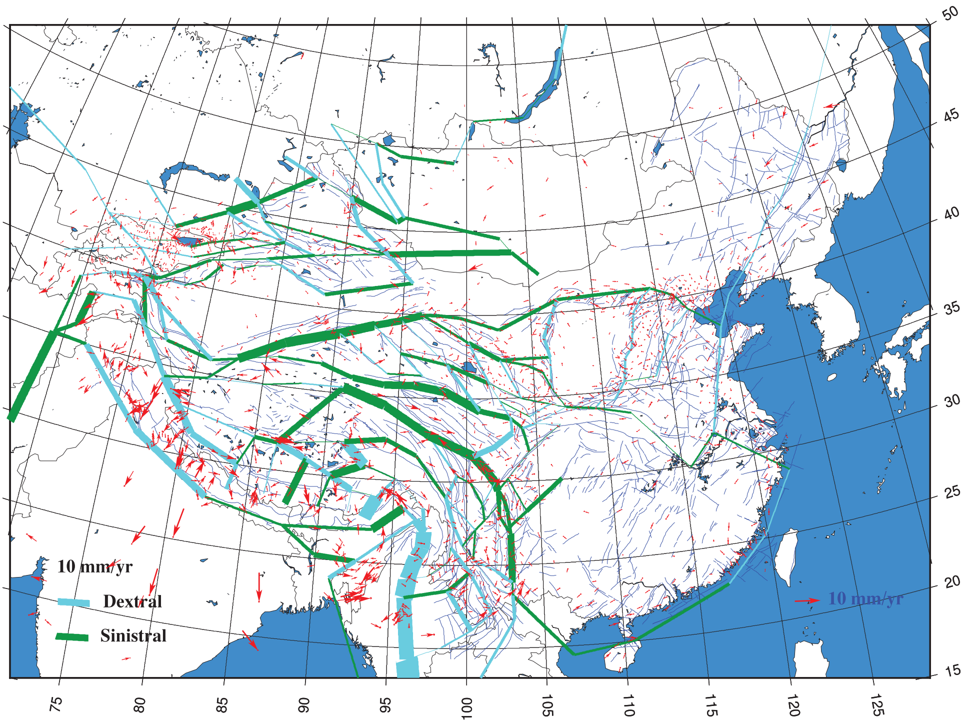

(a)

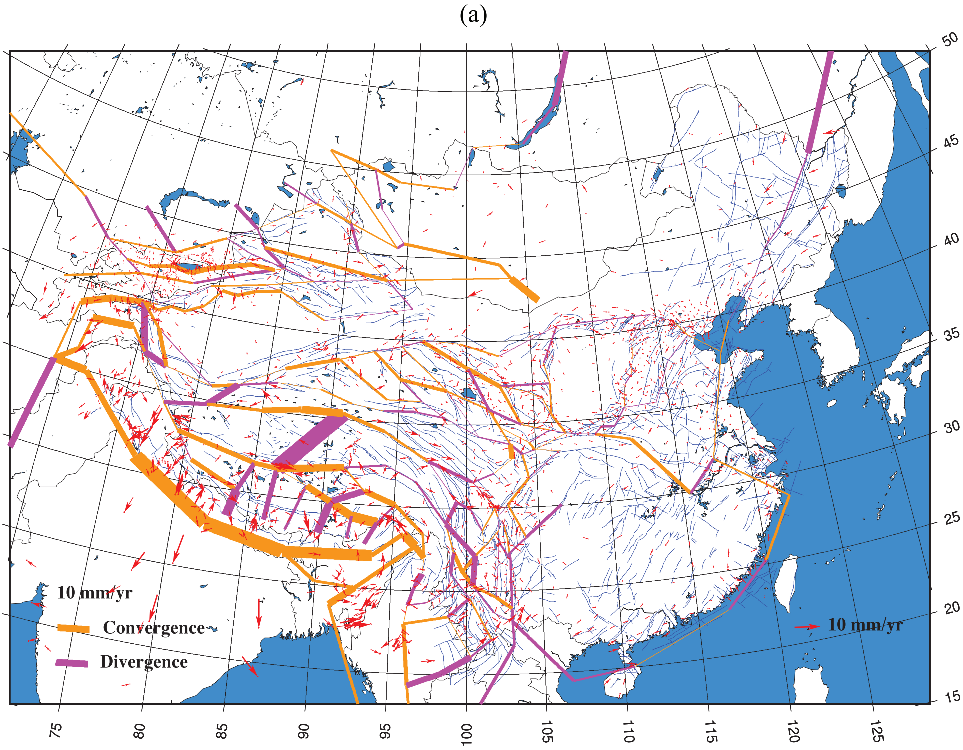

(b)

Figure 5. Inverted fault slip rates: (a) strike-slip component and (b) fault normal component. Thickness of the fault trace is proportional to fault slip rate, and the color represents the sense of slip. Red vectors are residual GPS velocities.

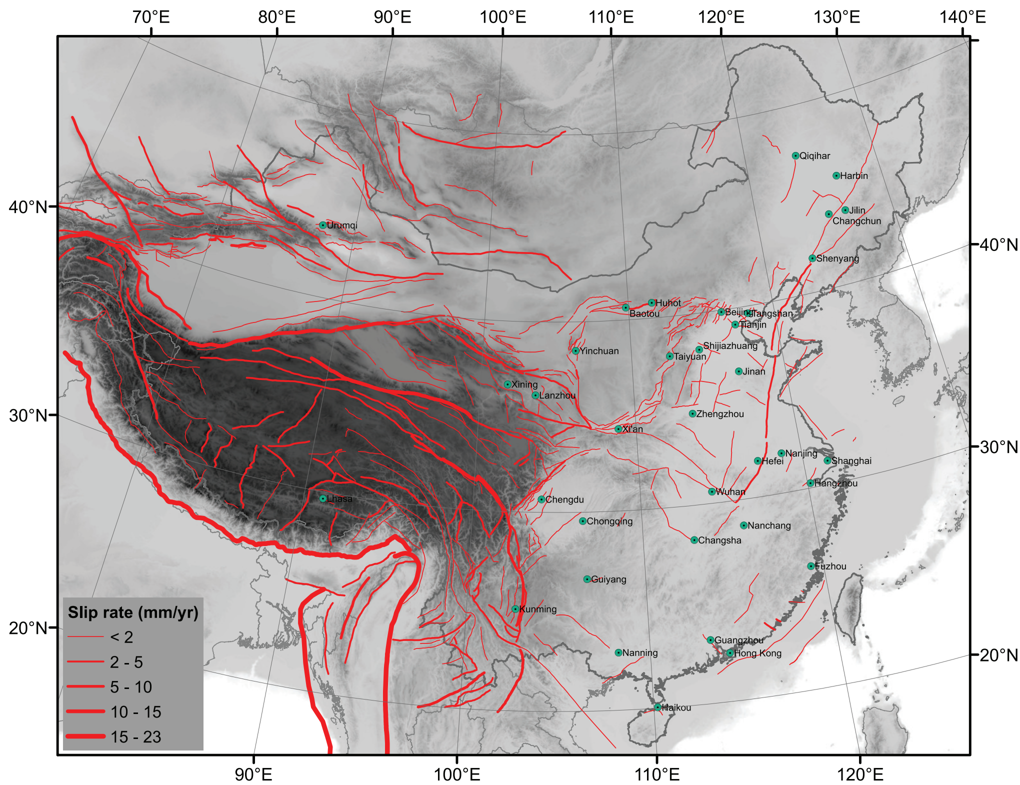

Figure 6. Final seismogenic fault sources (red lines) and their slip rates.

Modeling fault sources. In many seismic hazard analyses, earthquake magnitude–frequency distribution on faults are modeled using the characteristic model, which assumes that large characteristic earthquakes repeatedly rupture the same portion of the fault with a similar magnitude and slip distribution (Schwartz and Coppersmith, 1984; Wesnousky, 1994). Implementing the characteristic model into seismic hazard analysis is tempting because of its simplicity. However, the characteristic model has its limitations and its validity has been seriously challenged (Bird et al., 2010; Howell, 1985; Kagan, 1993; Kagan et al., 2012; Page and Felzer, 2015; Rong et al., 2003). Moreover, implementing a characteristic model requires the knowledge of fault segmentation, characteristic magnitude, and recurrence times, which may not be available or have large uncertainties.

Therefore, we characterize seismicity on the faults using fault dimensions and slip rates, and assume the occurrence of earthquakes follows a type of Gutenberg–Richter (GR) distribution (Anderson and Luco, 1983; Youngs and Coppersmith, 1985). In addition, we assume that the total seismic moment rate from the magnitude distribution equals the geological moment rate $\dot{M}_g$, which can be estimated by

$$\dot{M}_g = c\mu W L \bar{u} \tag{4}$$

where c is the seismic coupling coefficient of a fault, μ is the elastic shear modulus of the crust (a typical value is 30 GPa), W is the width of the fault, L is the length of the fault, and $\bar{u}$ is its slip rate.

We adopt truncated GR distributions for the earthquakes on faults and assume the GR b-value of earthquakes associated with a fault to be the same as the b-value of the seismic source zone containing the fault. The truncated GR distribution is the same as a regular GR distribution, except that in the truncated distribution, the earthquake rate for magnitudes larger than the maximum magnitude is zero. To use truncated GR distributions, we need to determine lower- and upper-bound magnitudes for each of the faults. The upper-bound magnitude can be inferred from fault length–earthquake magnitude scaling relationships. We collect the magnitude and rupture parameters of 91 earthquakes in mainland China and nearby regions to study magnitude–rupture scaling relations (Cheng et al., 2019). The relationships that we derive based on post-1900 earthquakes are not statistically different from the results derived using global datasets (Blaser et al., 2010; Wells and Coppersmith, 1994). Therefore, we choose the magnitude–rupture length scaling relationship by Wells and Coppersmith (1994) to infer the upper-bound magnitudes for faults and their magnitude–rupture area relationship for hazard calculation. In the hazard calculation, when the rupture area is smaller than the fault area, we allow the earthquake rupture to float along the fault plane (Pagani et al., 2014).

Characterizing earthquake occurrence for a seismic source zone. We employ a tapered Gutenberg–Richter (TGR) distribution to model earthquake magnitude–frequency distribution for each source zone. The TGR distribution has an exponential taper applied to the number of events of large seismic moment, which ensures a finite moment flux for a region. The TGR is most conveniently expressed in terms of seismic moment, M, instead of magnitude (M_W) (Kagan, 2002a):

$$F(M) = \alpha_t \left(\frac{M_t}{M}\right)^{\beta} \exp\left(\frac{M_t - M}{M_c}\right) \quad \text{for } M_t \leqslant M < \infty \tag{5}$$

where M is in N m, and $M = 10^{1.5M_W + 9.05}$ (Hanks and Kanamori, 1979). Here, $F(M)$ is the rate of earthquakes with moment larger than M, and β equals 2/3 of the GR b-value. M_c is called corner moment (the corresponding magnitude is called corner magnitude, m_c), which controls the distribution in the upper ranges of M. M_t is a threshold moment (the corresponding magnitude is threshold magnitude, m_t) above which the catalog is assumed to be complete, and α_t is the seismicity rate for earthquakes with moment M_t and greater. The difference between truncated GR and TGR distributions is that a truncated GR has a hard cutoff at the maximum magnitude, whereas a TGR slowly tapers off the earthquake rate.

The TGR parameters α_t and β can be determined based on historical earthquakes in a source zone. M_c can be estimated using the seismic moment conservation principle (Kagan, 2002a, 2002b):

$$M_c \simeq \left[\frac{\chi \dot{M}_{T0}(1-\beta)}{\alpha_t M_t{}^{\beta} \Gamma(2-\beta)}\right]^{1/(1-\beta)} \tag{6}$$

where $\dot{M}_{T0}$ is the total tectonic moment rate determined from geodetic or geologic measurements, χ is seismic coupling, and Γ is the gamma function. The tectonic moment rate that is assumed to be released by earthquakes is $\dot{M}_T = \chi \dot{M}_{T0}$.

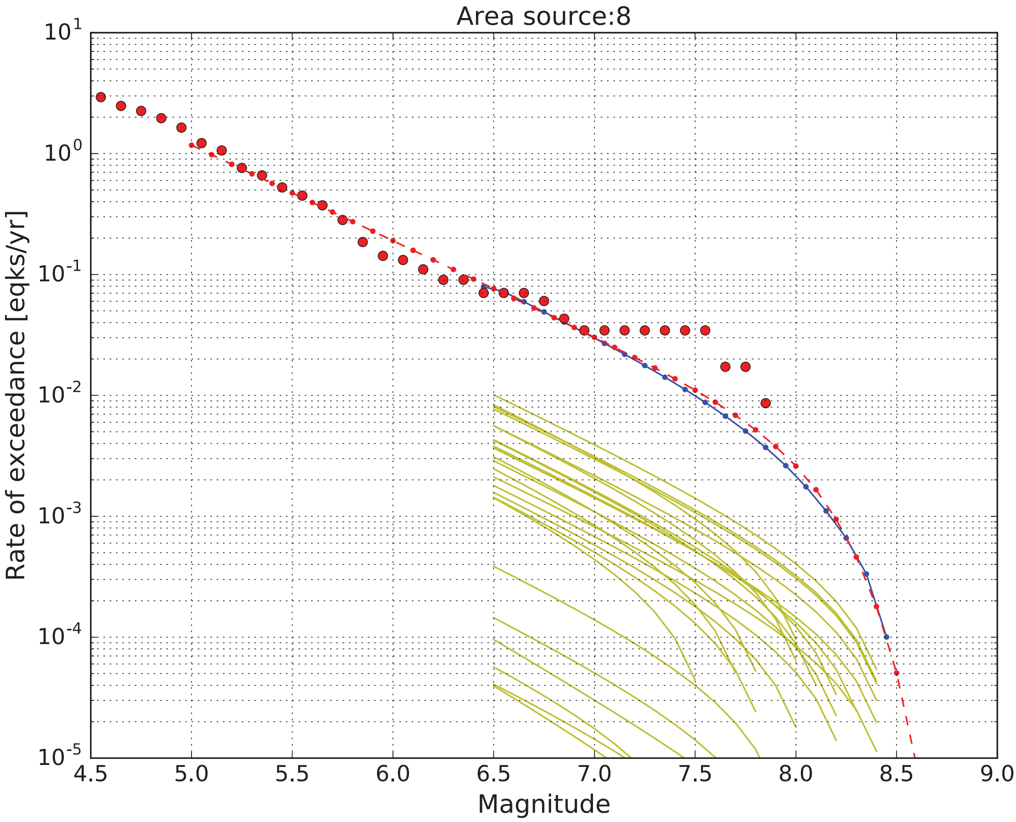

Figure 7. Cumulative magnitude–frequency distributions of source zone 8. The red dashed line shows the TGR distribution obtained using the historical earthquake catalog and strain rate map. The red dots show the magnitude–frequency distribution of historical seismicity. Yellow lines are the magnitude–frequency distributions obtained for the individual faults inside the zone; the blue curve shows the summed magnitude–frequency distribution of the individual faults. The difference between the blue and red curves is modeled as background seismicity.

We estimate $\dot{M}_T$ from the geodetic strain rate model using the method described in the study by Bird and Kreemer (2014). The tectonic moment rate of area A (such as one grid cell in the strain rate map) with uniform long-term permanent strain rate is

$$\dot{M}_T = A\chi z\mu \begin{cases} 2\dot{\varepsilon}_3; & \text{if } \dot{\varepsilon}_2 < 0 \\ -2\dot{\varepsilon}_1; & \text{if } \dot{\varepsilon}_2 > 0 \end{cases} \tag{7}$$

where $\dot{\varepsilon}_1$ and $\dot{\varepsilon}_3$ are the largest and smallest principal values, respectively; χ is seismic coupling, μ is the elastic shear modulus, and z is seismogenic thickness. The product of χ and z is called the coupled thickness of seismogenic lithosphere (Bird et al., 2010; Bird and Kreemer, 2014; Bird and Liu, 2007).

The obtained TGR relationship defines the total magnitude–frequency distribution for a source zone. We divide the total magnitude–frequency distribution into two parts: one part is attributed to the earthquakes on active faults and the rest to the background seismicity. Figure 7 demonstrates the cumulative magnitude–frequency distributions for source zone 8. In this study, we assume a lower-bound magnitude of 6.5 for the earthquakes on the active faults. Ideally, the magnitude range of earthquakes on each fault should be determined based on the characteristics of the fault, regional tectonics, and earthquake history. However, there are not enough earthquake data for identifying such magnitude ranges. For this zone, the modeled earthquake rate at large magnitude seems to deviate from observations. This deviation is caused by using 1900 as a completeness year for earthquakes between magnitude 6.7 and 7.8 (Table 1), but the real recurrence times for earthquakes with magnitude of 7.5 and larger may be much longer.

Characterizing background seismicity. After we have characterized earthquake occurrence for a source zone and for faults within that source zone, we attribute the difference between earthquake occurrences for the source zone and the faults to the background seismicity. We use a smoothed seismicity method to distribute the background seismicity, that is, the distribution of background seismicity is based on the off-fault magnitude–frequency distribution and spatial distribution of historical earthquakes. We use two Gaussian kernels (Frankel, 1995) in the smoothing process: a kernel of 50 km distance for distributing 80% seismicity and a kernel of 100 km for distributing 20% seismicity. Distributed seismicity is modeled on a regular grid of point sources covering the extent of the source zone. To avoid double counting contributions from both smoothed seismicity and fault sources, the magnitude–frequency distribution of point sources within a buffer around each fault source is truncated at the magnitude corresponding to the minimum magnitude of the magnitude–frequency distribution of the corresponding fault (M_W 6.5). Figure 7 illustrates the process using source zone 8 as an example.

Seismicity rates for shallow source zones. For crustal earthquakes, we delineate 25 large shallow source zones (Figure 2) based on seismotectonics illustrated in Figure 1. We attribute historical earthquakes with hypocentral depth less than 35 km as shallow events. We decluster the historical earthquake catalog using the method by Gardner and Knopoff (1974). For each of the zones, we determine the catalog completeness times based on the declustered catalog. The completeness times are first determined using an automated version of the Stepp methodology (Stepp, 1972) for western and eastern China. Then, we visually inspect a series of plots of earthquake magnitude versus time and cumulative number of earthquakes above a certain magnitude versus time. We use the slope changes in the plots to adjust the automatically determined completeness times. The final catalog completeness times are summarized in Table 1. We use M_W 7.4 and 7.9 instead of 7.5 and 8.0 as completeness magnitudes for the time period before 1900. This is because M_W 7.4 and 7.9 are converted from M_S 7.5 and 8.0, and the magnitudes of intensity-based historical earthquakes were reported at ¼ magnitude intervals. The table shows that the earthquakes are completely recorded at M_W 4.5 and above since 1985 for all the zones. For most of the zones in western China, the earthquake catalog is complete at M_W 6.7 since 1900, and M_W 7.9 since 1800. For most of the zones in eastern China, the earthquake catalog is complete at M_W 6.5 since 1650, and M_W 7.9 since 1550.

Next, we estimate the TGR b-value and a-value (and therefore β and α_t) using the Weichert method (Weichert, 1980) for each of the source zones (Table 2). In the calculation of tectonic moment rate using Equation 7, neither seismogenic thickness (z) nor seismic coupling (χ) are well determined. Most studies suggest a fault locking depth of 15–25 km (Wang et al., 2017; Zhang et al., 2013) for China. However, the locking depth may be as deep as 40 km for North China (Wang et al., 2011). Because the factor of 2 in Equation 7

Table 1. Completeness times (T) of the historical earthquake catalog for shallow source zones

Zone ID	T_1	M_{W1}	T_2	M_{W2}	T_3	M_{W3}	T_4	M_{W4}	T_5	M_{W5}	T_6	M_{W6}	T_7	M_{W7}
1	1985	4.5	1964	5.0	1950	5.5	1930	5.7	1900	6.9	1820	6.7	1800	7.9
2	1985	4.5	1966	5.0	1928	5.3	1917	5.7	1916	6.1	1900	6.7	1800	7.9
3	1985	4.5	1966	5.0	1917	5.3	1905	5.7	1900	6.5	1650	7.4	1550	7.9
4	1985	4.5	1966	5.0	1950	5.3	1923	5.7	1916	6.1	1900	6.7	1800	7.9
5	1985	4.5	1976	5.0	1968	5.1	1920	5.2	1920	5.3	1600	6.5	1550	7.9
6	1985	4.5	1966	5.0	1917	5.3	1905	5.7	1630	6.4	1600	7.4	1550	7.9
7	1985	4.5	1966	5.0	1940	5.3	1930	5.7	1905	6.1	1850	6.7	1750	7.9
8	1985	4.5	1966	5.0	1950	5.3	1923	5.7	1916	6.1	1900	6.7	1800	7.9
9	1985	4.5	1966	5.0	1928	5.3	1917	5.7	1916	6.1	1900	6.7	1800	7.9
10	1985	4.5	1980	5.0	1960	5.2	1920	5.7	1900	6.5	1650	7.4	1550	7.9
11	1985	4.5	1966	5.0	1950	5.1	1930	5.5	1920	6.0	1900	6.7	1800	7.9
12	1985	4.5	1966	5.0	1909	5.3	1905	5.7	1900	6.5	1650	7.4	1550	7.9
13	1985	4.5	1966	5.0	1917	5.3	1800	5.7	1600	6.0	1400	6.6	1300	7.8
14	1985	4.5	1966	5.0	1917	5.3	1905	5.7	1900	6.5	1650	7.4	1550	7.9
15	1985	4.5	1966	5.0	1935	5.3	1923	5.7	1916	6.1	1905	6.7	1800	7.9
16	1985	4.5	1966	5.0	1966	5.1	1938	5.5	1916	6.0	1890	6.3	1870	6.7
17	1985	4.5	1966	5.0	1917	5.3	1905	5.7	1900	6.5	1650	7.4	1550	7.9
18	1985	4.5	1966	5.0	1928	5.3	1917	5.7	1916	6.1	1900	6.7	1800	7.9
19	1985	4.5	1966	5.0	1917	5.3	1905	5.7	1900	6.5	1650	7.4	1550	7.9
20	1985	4.5	1966	5.0	1917	5.3	1905	5.7	1900	6.5	1650	7.4	1550	7.9
21	1985	4.5	1966	5.0	1928	5.3	1917	5.7	1916	6.1	1900	6.4	1500	7.6
22	1985	4.5	1966	5.0	1950	5.3	1950	5.7	1910	6.1	1910	6.7	1800	7.9
23	1985	4.5	1966	5.0	1917	5.3	1905	5.7	1900	6.5	1650	7.4	1550	7.9
24	1985	4.5	1966	5.0	1917	5.3	1905	5.7	1900	6.5	1650	7.4	1550	7.9
25	1985	4.5	1966	5.0	1917	5.3	1905	5.7	1900	6.5	1650	7.4	1550	7.9

Table 2. Derived seismic parameters for each shallow seismic source zone

Zone ID	*a*-value	*b*-value	Coupled thickness (km)	$\dot{M}_{T0}$(N m)	m_c	*c* (fault coupling)
1	4.65	0.86	40	6.41E+19	9.14	0.8 for crustal faults; 0.3 for Indo-Burman subduction
2	4.10	0.80	20	1.38E+19	8.17	1.0
3	3.60	0.69	25	1.15E+19	7.66	1.0
4	4.52	0.82	15	1.16E+19	7.74	1.0
5	4.99	1.09	15	1.44E+18	8.90	1.0
6	4.21	0.91	20	2.61E+18	8.22	1.0
7	5.20	0.93	50	1.02E+20	9.58	0.5 for Himalaya frontal fault; 1.0 for other faults
8	4.02	0.79	20	1.28E+19	8.16	0.7
9	4.77	0.97	15	3.44E+18	8.21	0.3
10	3.76	0.81	25	4.32E+18	8.05	0.6
11	3.84	0.84	25	4.21E+18	8.22	0.4
12	3.28	0.74	20	4.77E+18	8.03	1.0
13	3.48	0.81	30	2.25E+18	8.03	0.8
14	3.34	0.78	20	1.95E+18	7.90	1.0
15	5.13	0.93	15	2.36E+19	8.47	1.0
16	5.27	0.95	25	2.21E+19	8.44	1.0
17	4.02	0.98	15	1.13E+18	8.82	1.0
18	4.66	0.89	15	1.44E+19	8.36	1.0
19	4.38	1.01	25	1.70E+18	8.90	1.0
20	4.11	0.92	15	1.25E+18	7.87	1.0
21	4.34	0.83	15	1.08E+19	8.03	1.0
22	2.92	0.68	25	3.18E+18	7.74	1.0
23	3.48	0.77	15	3.57E+18	7.93	1.0
24	3.59	0.80	15	4.49E+18	8.25	1.0
25	3.71	0.83	15	1.62E+18	7.78	1.0

comes from the assumption that the fault planes have angles of 45° with the principal strain-rate axis, for an area dominated by vertical faults the effective value of z in Equation 7 should be smaller than fault locking depth, and for the zones with many shallow dipping faults the effective value of z should be larger than the locking depth. Based on the seismogenic thicknesses estimated in the literature, major faulting mechanisms, and the characteristics and rates of seismicity in each zone, we assign the coupled thickness (Table 2). The coupled thickness is large for zones 1 and 7 because of the shallow dip of the faults in the subduction environment.

We adopt a locking depth of 15 km to calculate the geological moment rates for seismogenic fault sources. While we use the rupture length–magnitude relationship by Wells and Coppersmith (1994) to determine upper-bound magnitudes for the fault sources, we add 2σ to the mean magnitudes to capture the uncertainties. For the faults that run into more than one source zone, we partition its magnitude–frequency distribution into the different zones according to the proportion of the fault length falling into each zone. For some zones that contain fast-slipping long faults, the total fault-based magnitude–frequency distributions may be much higher than the TGR determined by the historical earthquake data and strain rate model. In these cases, we consider fault coupling coefficients of less than 1.0. The coupling coefficients are determined by matching the total fault-based magnitude–frequency distributions with the TGR at magnitude of 6.6. The fault coupling coefficients are reported in Table 2. We assume that the fault coupling is the same for all

Table 3. Catalog completeness times (T) for deep earthquakes

Layer depth (km)	T_1	M_{W1}	T_2	M_{W2}	T_3	M_{W3}	T_4	M_{W4}	T_5	M_{W5}
35–70	1985	5.0	1970	5.3	1923	5.6	1900	6.6	1800	7.9
70–150	1985	4.5	1980	4.7	1970	5.0	1964	5.7	1900	7.0
150–300	1980	4.7	1970	5.0	1964	5.5	1900	6.7	1880	7.0
300–700	1985	4.5	1964	5.5	1923	6.0	1900	6.6	1800	7.9

the faults within a zone with the exceptions of zones 1 and 7. For zone 1, the oblique convergence rate of Indo-Burman subduction is high. However, most of the large earthquakes occurred on crustal faults. Therefore, we assign a lower coupling for the subduction fault. For zone 7, since the hazard is dominated by the Himalaya frontal fault, we assign a coupling coefficient to this fault only.

Seismicity rates for deep source zones

Deep earthquakes occur in some regions in and around China. We delineate deep source zones for different depth layers (Figure 8). The catalog completeness times for each layer (Table 3) are determined by the Stepp methodology (Stepp, 1972). A truncated GR relationship is used to model the seismicity rate for each of the zones. The GR a- and b-values (Table 4) are determined from the declustered historical earthquake catalog using the Weichert method (Weichert, 1980). The upper-bound earthquake magnitude for each zone is set as the largest observed earthquake magnitude plus 0.5 unit. A simple smoothed seismicity method is used to model the seismicity rates at each grid point in a source zone. Note that the b-value of the 300–700 km deep source zone is only 0.4, which may hint that at that depth smaller earthquakes are below the detection threshold of the seismic networks. We do not manually inspect the catalog completeness times for this zone since the earthquakes are too deep to have significant contribution to the hazard.

Seismic hazard modeling

Selection of GMMs

The fifth-generation seismic ground motion parameters zonation map (General Administration of Quality Supervision, Inspection and Quarantine of the People's Republic of China, 2015) used the GMMs by Yu et al. (2013) (YLX13). Those GMMs were developed for surface wave magnitude, M_S, and provided relationships only for PGA and peak ground velocity. We evaluate five GMMs from the NGA-West2 project (Bozorgnia et al., 2014) for shallow crustal earthquakes: ASK14 (Abrahamson et al., 2014), BSSA14 (Boore et al., 2014), CB14 (Campbell and Bozorgnia, 2014), CY14 (Chiou and Youngs, 2014), and IM14 (Idriss, 2014). We choose them because (1) they are based on the most extensive collection of earthquake recordings from tectonically active regions, including several earthquakes in China, (2) they were recently developed by experienced teams and are recognized as state-of-the-art, and (3) the Q values between much of China and California indicate similar tectonic environments (Dangkua et al., 2018 and references therein). In addition, four of five of the NGA-West2 GMMs proposed specific regional attenuation adjustments for China.

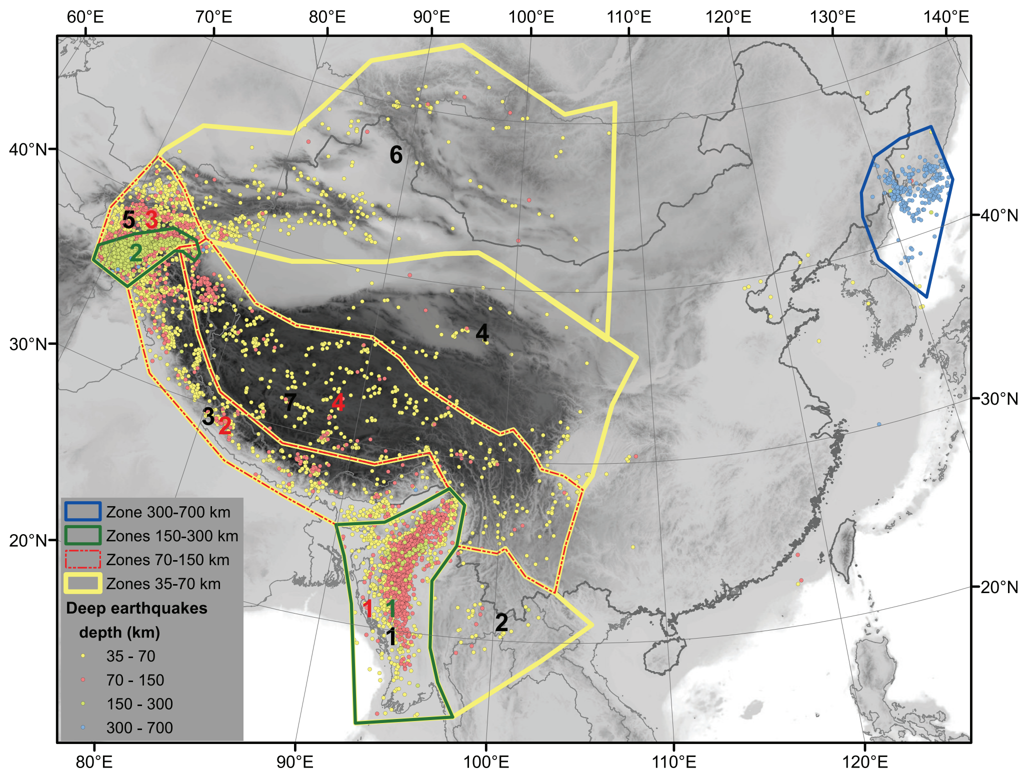

Figure 8. Deep seismic source zones (polygons with different colors representing different depth layers; their IDs are labeled using the corresponding color except that the 35–70 km layer is labeled in black). Note that the zone of 300–700 km depth is not numbered since there is only one zone in that depth layer. Circles show historical earthquakes ($M_W \geqslant 4.0$ only, colored by depth).

We collect ~1500 ground motion observations from earthquakes in and around China with a magnitude range from 4.0 to 7.9 and source-to-site distances up to 1500 km and analyze residuals for PGA and spectra accelerations (SA) at 0.2–2.0 s to quantitatively compare instrumentally recorded ground motions and values predicted by the GMMs. For PGA, all the NGA-West2 models perform better than the YLX13. For PGA and SA 0.2 s, the NGA-West2 GMMs are generally consistent with the observed data with BSSA14 performing the best and IM14 the worst. For SA 1.0 s, all the NGA-West2 GMMs predict higher ground motion than the observed data. Predicted ground motions from IM14 show the closest agreement with the observed long-period data.

Based on the analysis, we assign equal weights to ASK14, BSSA14, CB14, CY14, and IM14 for PGA and SA 0.2 s, and various weights for longer period SAs (Table 5). The details on GMM selection and weights can be found in Dangkua et al. (2018).

For deep earthquakes, we do not have ground motion data for selecting GMMs. We adopt the Zhao et al. (2006) GMM for in-slab and deep events. The GMM has been ranked as one of the best models for seismic hazard analysis (Bommer et al., 2010), and it was widely employed to model seismic hazard for subduction and deep earthquakes (e.g. Petersen et al., 2015; Woessner et al., 2015).

Table 4. Derived GR parameters for each deep source zone

Layer depth (km)	Zone ID	*a*-value	*b*-value
35–70	1	6.14	1.16
	2	3.01	0.70
	3	7.47	1.47
	4	4.38	1.11
	5	8.65	1.68
	6	4.49	0.91
	7	5.54	1.16
70–150	1	5.60	1.05
	2	4.16	0.95
	3	5.92	1.09
	4	4.54	1.02
150–300	1	6.06	1.37
	2	3.46	0.66
300–700	1	1.92	0.40

GR: Gutenberg–Richter.

Table 5. Recommended weights for each GMM for crustal earthquakes (Dangkua et al., 2018)

	ASK14	BSSA14	CB14	CY14	IM14
Overall	0.25	0.15	0.2	0.15	0.25
PGA	0.2	0.2	0.2	0.2	0.2
SA 0.2 s	0.2	0.2	0.2	0.2	0.2
SA 0.5 s	0.2	0.15	0.2	0.2	0.25
SA 1.0 s	0.25	0.125	0.2	0.125	0.3
SA 2.0 s	0.2	0.1	0.2	0.1	0.4

GMM: ground motion model; PGA: peak ground acceleration.

Seismic site condition map

Because ground motions can be significantly amplified (or de-amplified) by seismic site conditions, we develop a site condition map for mainland China using geology as a proxy to define the National Earthquake Hazards Reduction Program (NEHRP) site categories (Wills and Clahan, 2006; Wills et al., 2000, 2015). We obtain the geology information from two sources: a bedrock geology database with a scale of 1:1,000,000 (Ding et al., 2011), and a Quaternary map with a scale of 1:2,500,000 (Zhang et al., 1990). The bedrock geology database has more detail on bedrock conditions than the Quaternary map, and the Quaternary map has more detail on soils than the geology map. We assign the NEHRP site categories to each geologic unit using the age, genesis, and lithologic descriptions in both maps, and thus, we produce two versions of site condition map. The final map (Figure 9) is a result of integrating the two versions of the site condition map: using the results from the bedrock geology database for bedrock areas and the results from the Quaternary map for soil-covered areas. The details on the development of the map will be documented in a future publication.

Seismic hazard maps

The seismic hazard is calculated using the OpenQuake engine (Pagani et al., 2014). Logic trees are implemented for GMMs based on Table 5. For focal depths and mechanisms in

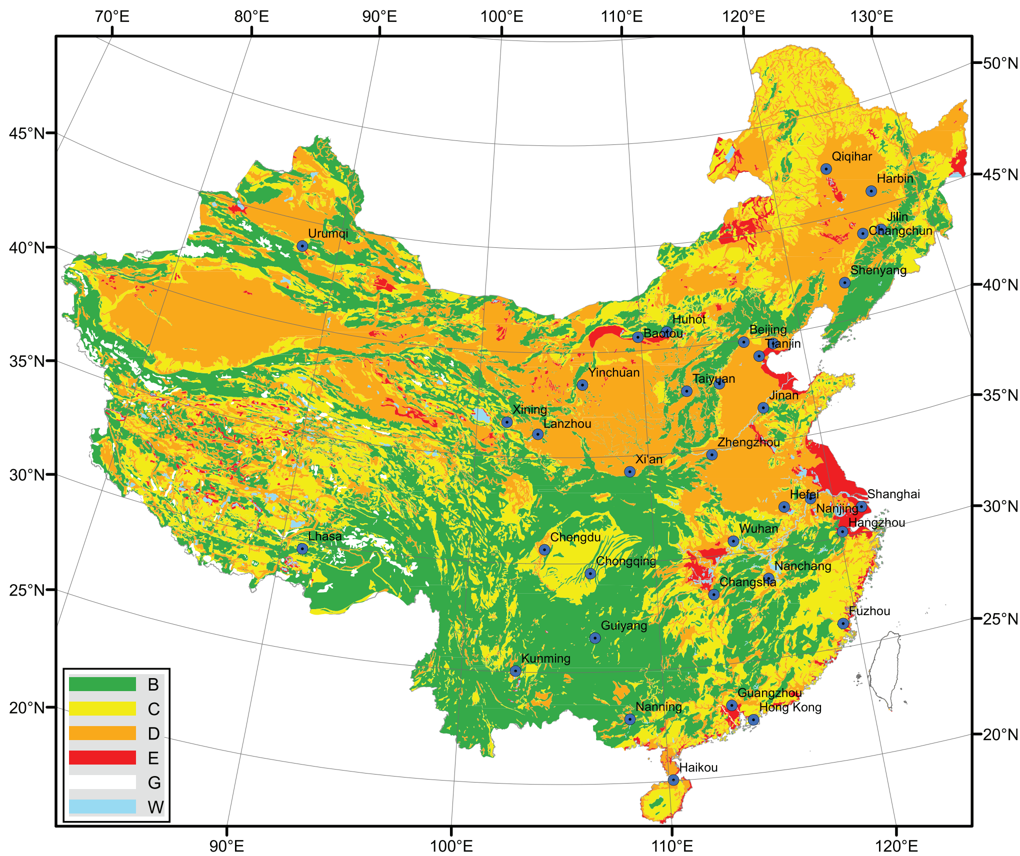

Figure 9. Seismic site condition map integrated from the bedrock geology database and the Quaternary map. B, C, D, and E are NEHRP categories, W is water, and G is glacier.

seismicity modeling, the logic trees are based on the statistics of historical earthquakes in each source zone. Figures 10a to c display the 500-year return period PGA, and SA at 0.2 and 1.0 s for rock site condition (V_{S30} = 760 m/s, or NEHRP BC). Figure 10d illustrates the 500-year return period SA at 1.0 s after site amplification factors (Seyhan and Stewart, 2014) are applied. Seismic hazard is greatly amplified in many regions with soft deposits (Figure 9), including some large cities such as Shanghai, Guangzhou, and Tianjin (compare Figure 10d with Figure 10c). Figure 11 illustrates the hazard curves of SA 0.2 s on rock site condition for selected cities (cities are labeled in Figures 6, 9, and 10d). Kunming has the highest seismic hazard in the selected cities because Kunming is surrounded by many active faults, including the Xianshuihe–Xiaojiang fault system (Figure 6). Wuhan, located in the relatively stable South China block, has the lowest hazard.

Comparison with the fifth-generation seismic zonation map of China

The PGA values shown in the fifth-generation seismic ground motion parameters zonation map are the larger of 500- and 2500-year PGA divided by a factor of 1.9, where the factor 1.9 is the average ratio between 2500- and 500-year PGA values determined from the model (Gao, 2015). The map shows only six PGA category values: 0.05g, 0.10g, 0.15g,

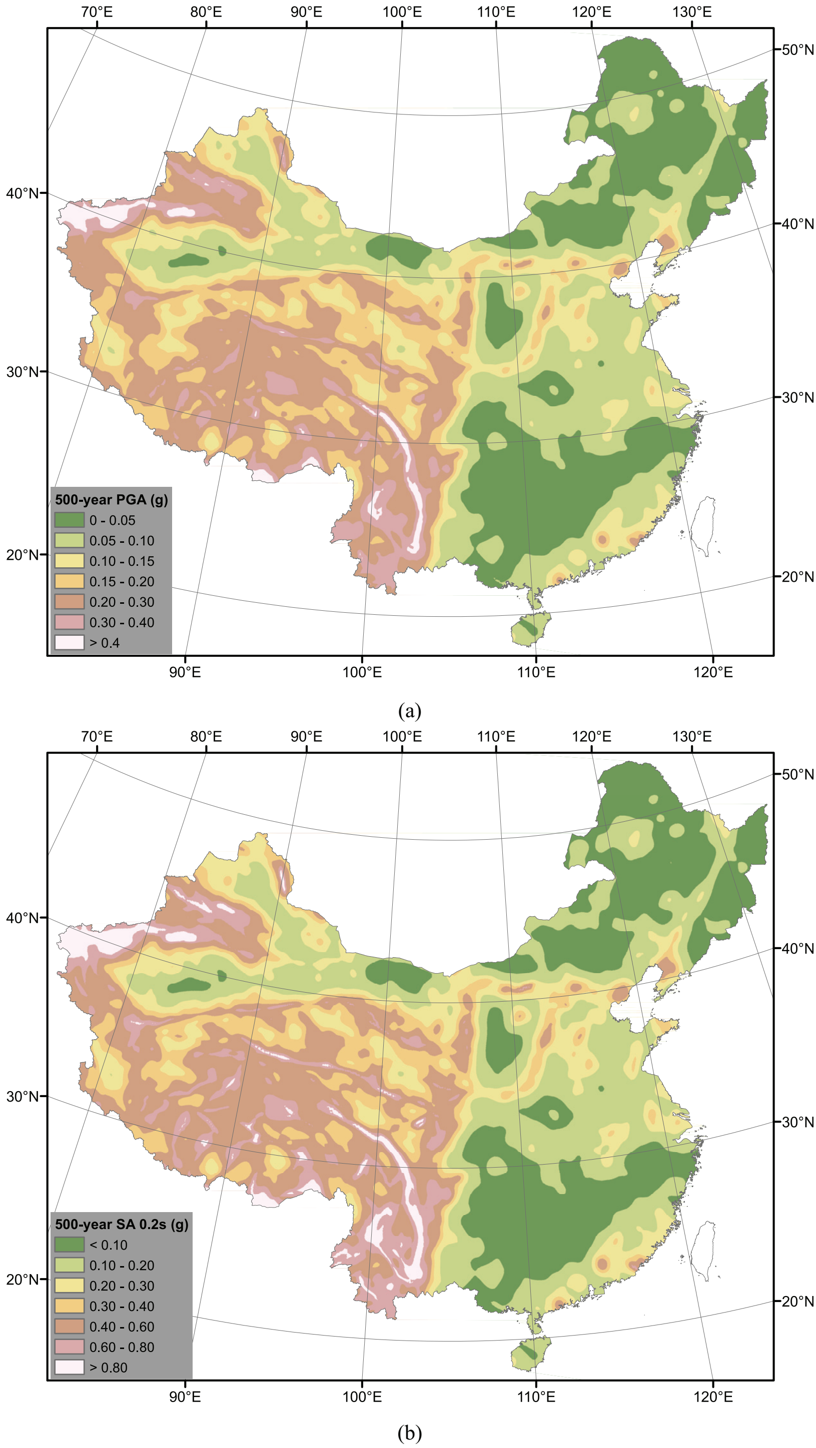

Figure 10. Seismic hazard maps for mainland China. (a) 500-year PGA, (b) 500-year SA at 0.2 s, and (c) 500-year SA at 1.0 s for rock site condition, and (d) 500-year SA at 1.0 s amplified by site conditions. Ground motion scales vary in each panel.

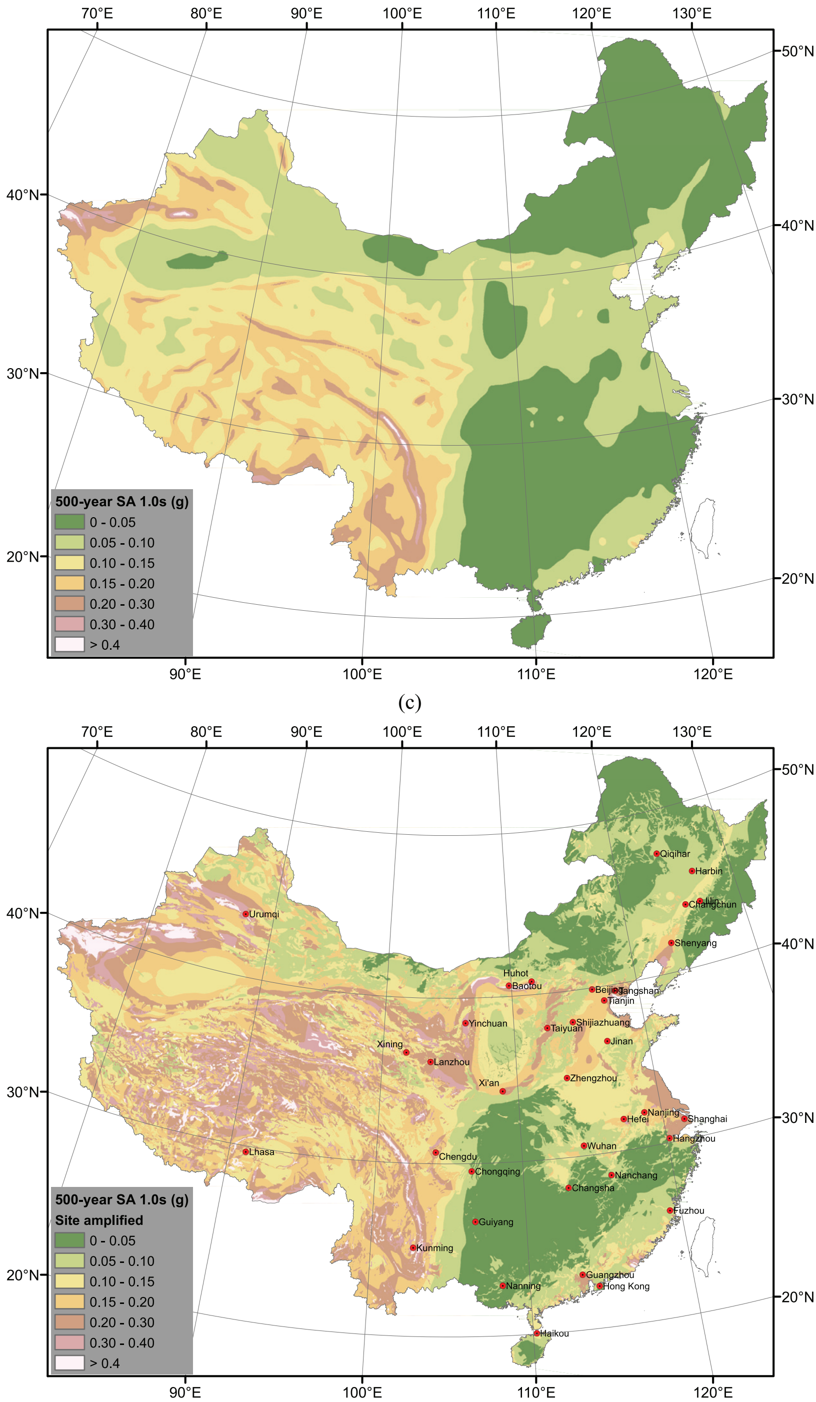

(c)

(d)

Figure 10. (continued)

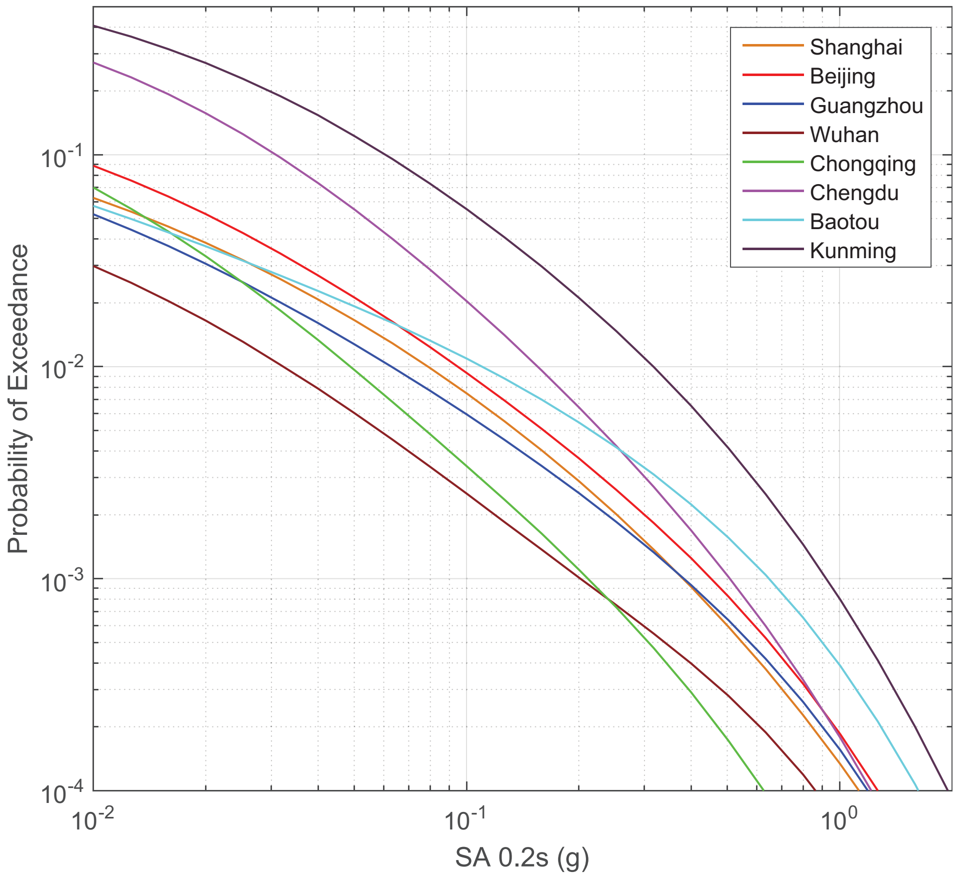

Figure 11. Hazard curves of SA 0.2 s at selected cities on rock site condition.

0.20g, 0.30g, and 0.40g; however, each PGA value represents a range of PGAs and corresponds to a modified Mercalli intensity (MMI) scale value. Moreover, the PGA values are relative to the Chinese Class II site category, which straddles the NEHRP C and D boundary (Lü and Zhao, 2007).

To compare our hazard results with the fifth-generation map, we also calculate the larger of 500-year PGA and 2500-year PGA divided by a factor of 1.9 for NEHRP BC site condition. Because Chinese site class I_1 is deemed as rock site condition and is close to NEHRP BC, we convert the fifth-generation seismic ground motion PGA values from China site Class II to values relative to Chinese site class I_1 using the coefficients provided by the national standard (General Administration of Quality Supervision, Inspection and Quarantine of the People's Republic of China, 2015). Figure 12 illustrates the comparison. For 26 out of 36 cities shown in Figure 12, the values from our model and those from China fifth-generation map are consistent within one-standard error. The largest discrepancy is seen for Haikou, the capital city of Hainan province. A large earthquake in 1605 struck the northern region of the Hainan Island. The magnitude of the earthquake was estimated to be 7–7.5 based on intensities. However, the damage was a cumulative effect of a sequence of earthquakes, liquefaction, and flooding associated with a typhoon (Jin and Wang, 1988). In

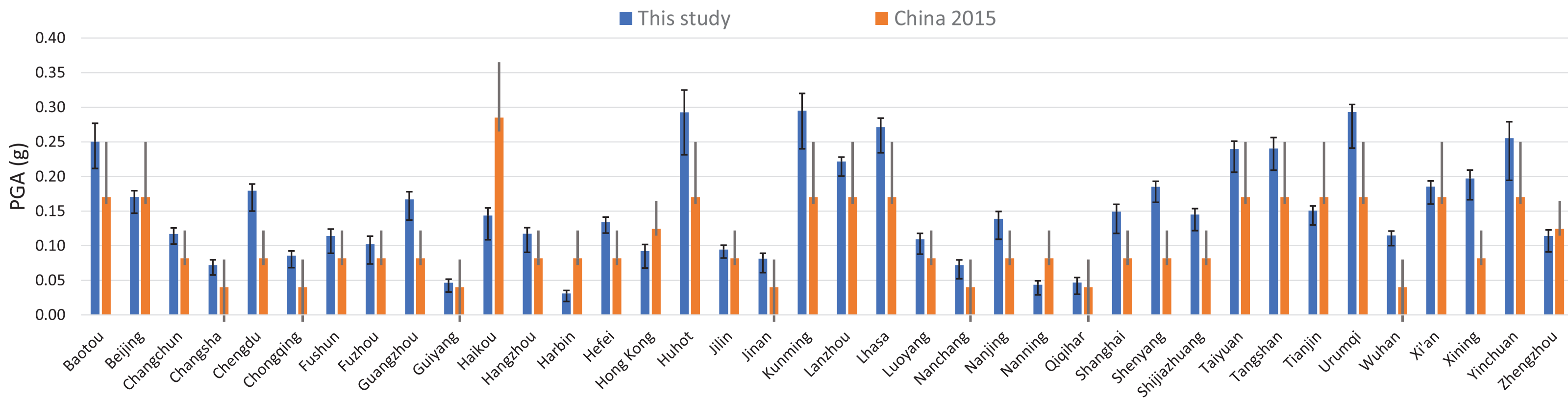

Figure 12. Comparison of PGA values from our model (blue bars, relative to rock site condition) and China fifth-generation map (orange bars, relative to Chinese site class I_1) for major cities. The black bars on blue bars show the 16th to 84th percentile values from our model. The gray bars on orange bars show the range of PGA values that correspond to an MMI unit.

addition, no earthquakes greater than magnitude 5 has been recorded in the area since 1920. We suspect that China fifth-generation map heavily weighed the 1605 event for the region.

The differences between our hazard results and China fifth-generation map can be attributed to the following aspects:

- *Different data and GMMs*. The China fifth-generation map used an M_S-based earthquake catalog and information on about 130 active faults, but strain rate data were not used. We use a newly compiled M_W-based catalog, about 500 active faults, and strain rate data. The fifth-generation map used YLX13 GMMs, while we adopt NGA-West2 GMMs.
- *Different modeling methodologies*. The fifth-generation national map delineated three tiers with a total of 1206 seismic source zones. Truncated GR was used to model magnitude–frequency distribution. The parameters of truncated GR were holistically determined using both objective information such as historical earthquakes, active faults, and seismotectonics, and subjective factors such as expert opinion. We delineate large source zones and model the earthquake rates by integrating historical earthquakes, active faults, and geodetic strain rate data.

Summary and discussion

We have developed a new seismic hazard model for mainland China. In the process of modeling seismicity:

- A linked-fault network model was developed to model fault slip rates using GPS data, and the modeled slip rates were used to supplement those collected from the literature;
- For each seismic source zone, the total seismicity rates were modeled by a TGR magnitude–frequency relationship, and then the total seismicity rates were partitioned to background and active faults;
- Geodetic strain rate was used to constrain the corner magnitude of TGR magnitude–frequency relationship for each source zone; and
- The seismicity on active faults was modeled using truncated GR instead of characteristic earthquake distribution.

We employed the GMMs from the NGA-West2 project to calculate ground shaking for crustal earthquakes and used the OpenQuake engine to perform the hazard calculation for rock site conditions. For most of the major cities, our hazard result is generally consistent with the fifth-generation seismic ground motion parameters zonation map of China. We accounted for site conditions using a geology-based NEHRP site condition map. The seismic hazard for soft soil sites is greatly amplified, especially for the long-period ground motions.

The CSEP experiment demonstrated that using geodetic strain rate in earthquake activity rate modeling is promising (Schorlemmer et al., 2018). Strain rate has been used for constraining earthquake rates in our earlier studies (Rong et al., 2014, 2016). However, the coupled thickness parameter used to quantify tectonic moment rate from strain rate is relatively uncertain. Since most of the studies in the literature suggest a locking depth of 15–25 km for China, we assigned the coupled thickness within this range for most of the zones. In the future, more rigorous study is needed to constrain the parameter. Another parameter which is also critical but difficult to determine is the fault coupling. In this study, the same fault coupling was given to all the faults in a seismic source zone. The fault coupling of 1.0 was assigned to the faults in most of the source zones. However, if the fault-based earthquake rate is higher than the TGR rate for the zone, we calculated the fault coupling by matching the earthquake rates. We believe this method of assigning coupling is better than assigning coupling to individual faults because it is more difficult to determine the coupling for individual faults.

Modeling seismic hazard in low seismicity areas remains challenging. Both crustal deformation and seismicity rate are low in the South China block (Zone 5 in Figure 2). Our data show that the geodetic-based moment rate is much larger than moment rates based on historical earthquakes or geological faults, manifested by the large corner magnitude shown in Table 2. More studies are needed to examine whether such a large corner magnitude is feasible. Nonetheless, the 500-year PGA and SA at 1.0 s for rock site condition is lower than 0.05g for this region (Figure 10).

We incorporated more than 500 active fault sources in the model. Due to the lack of information on fault parameters, we used a linked-fault network model to invert slip rate for faults. The accuracy of the results is limited by the model and its underlying assumptions, as well as the density of the GPS stations and the quality of the GPS data. The model cannot solve slip rate for each of the individual fault sources due to the sparsity of GPS stations in western China and the low deformation rate in eastern China. Since the total earthquake occurrence rate for each source zone was derived from historical earthquakes and strain rate data, the earthquake occurrence rate for an area with missing faults can be remediated using distributed seismicity. Nevertheless, the fault data need to be improved. We used an arbitrary magnitude of 6.5 as minimum magnitude when distributing earthquake rates on faults. This parameter can be modified if paleoseismic data are available and used in the modeling. Although we employed GR magnitude–frequency distributions to model earthquake occurrence on faults, the characteristic model is still being used by many seismic hazard models. Choosing characteristic or GR distributions will have impact on seismic hazard.

Another challenge in PSHA is to incorporate all sources of uncertainties in the model using a probabilistic approach. One of the advantages of using the OpenQuake engine is that one can easily apply logic trees to source models and GMMs. We implemented logic trees to capture the uncertainties in the GMMs and the focal depth and mechanism distributions in seismic sources. However, uncertainties in other input data (such as magnitudes of historical earthquakes, strain rate, and fault slip rates) and derived modeling parameters (magnitude–frequency distributions) need to be explicitly incorporated in hazard calculations in the future.

Acknowledgments

The authors are grateful to Marco Pagani for the collaboration of developing the seismic hazard modeling toolkit that was used to generate seismicity models for this work. The authors thank Sait A. Binselam for digitizing the Quaternary geological map, Donny T. Dangkua for the ground motion model selection study, and Jared Ogle for GIS help. The authors thank three anonymous reviewers, Editor Marco Pagani, and Editor-in-Chief David Wald for their constructive comments. The authors thank Hosam Ali, Franco Tamanini, and Lou Gritzo for reviewing the work and providing constructive comments.

Declaration of conflicting interests

The author(s) declared no potential conflicts of interest with respect to the research, authorship, and/or publication of this article.

Funding

The author(s) disclosed receipt of the following financial support for the research, authorship, and/or publication of this article: This project was supported by the Factory Mutual Insurance Company.

References

Abrahamson NA, Silva WJ and Kamai R (2014) Summary of the ASK14 ground-motion relation for active crustal regions. *Earthquake Spectra* 30: 1025–1055.

Anderson JG and Luco JE (1983) Consequences of slip rate constraints on earthquake recurrence relations. *Bulletin of Seismological Society of America* 73: 471–496.

Banerjee P, Bürgmann R, Nagarajan B and Apel E (2008) Intraplate deformation of the Indian subcontinent. *Geophysical Research Letters* 35. DOI: 10.1029/2008GL035468.

Bird P and Kreemer C (2014) Revised tectonic forecast of global shallow seismicity based on version 2.1 of the Global Strain Rate Map. *Bulletin of Seismological Society of America* 105: 152–166.

Bird P and Liu Z (2007) Seismic hazard inferred from tectonics: California. *Seismological Research Letters* 78: 37–48.

Bird P, Kreemer C and Holt WE (2010) A long-term forecast of shallow seismicity based on the Global Strain Rate Map. *Seismological Research Letter* 81: 184–194.

Blaser L, Kruger F, Ohrnberger M and Scherbaum F (2010) Scaling relations of earthquake source parameter estimates with special focus on subduction environment. *Bulletin of the Seismological Society of America* 100: 2914–2926.

Bommer JJ, Douglas J, Scherbaum F, Cotton F, Bungum H and Faäh D (2010) On the selection of ground-motion prediction equations for seismic hazard analysis. *Seismological Research Letters* 81: 783–793.

Boore DM, Stewart JP, Seyhan E and Atkinson GM (2014) NGA-West2 equations for predicting PGA, PGV, and 5% damped PSA for shallow crustal earthquakes. *Earthquake Spectra* 30: 1057–1085.

Bozorgnia Y, Abrahamson NA, Atik LA, Ancheta TD, Atkinson GM, Baker JW, Baltay A, Boore DM, Campbell KW and Chiou BS-J (2014) NGA-West2 research project. *Earthquake Spectra* 30: 973–987.

Calais E, Vergnolle M, Sankov V, Lukhnev V, Miroshnitchenko A, Amarjargal S and Deverchere J (2003) GPS measurements of crustal deformation in the Baikal-Mongolia area (1994-2002): Implications for current kinematics of Asia. *Journal of Geophysical Research* 108. DOI: 10.1029/2002JB002373.

Campbell KW and Bozorgnia Y (2014) NGA-West2 ground motion model for the average horizontal components of PGA, PGV, and 5% damped linear acceleration response spectra. *Earthquake Spectra* 30: 1087–1115.

Cheng J, Rong Y, Magistrale H, Chen G and Xu X (2017) An Mw-based historical earthquake catalog for mainland China. *Bulletin of Seismological Society of America* 107: 2490–2500.

Cheng J, Rong Y, Magistrale H, Chen G and Xu X (2019) Earthquake rupture scaling relations for mainland China. *Seismological Research Letters* 91: 248–261.

Chiou BS-J and Youngs RR (2014) Update of the Chiou and Youngs NGA model for the average horizontal component of peak ground motion and response spectra. *Earthquake Spectra* 30: 1117–1153.

Dangkua DT, Rong Y and Magistrale H (2018) Evaluation of NGA-West2 and Chinese ground motion prediction equations for developing seismic hazard maps of Mainland China. *Bulletin of the Seismological Society of America* 108: 2422–2443.

Devachandra M, Kundu B, Catherine J, Kumar A and Gahalaut VK (2014) Global Positioning System (GPS) measurements of crustal deformation across the Frontal Eastern Himalayan syntaxis and seismic hazard assessment. *Bulletin of the Seismological Society of America* 104: 1518–1524.

Ding X, Li T, Fan B, Yao D and Zhang Q (2011) *1:1,000,000 Geology Database of China*. Beijing, China: Institute of Geology, Chinese Academy of Geological Sciences.

Frankel A (1995) Mapping seismic hazard in the Central and Eastern United States. *Seismological Research Letters* 66: 8–21.

Fujiwara H, Kawai S, Aoi S, Morikawa N, Senna S, Kobayashi K, Ishii T, Okumura T and Hayakawa Y (2006) National seismic hazard maps of Japan. *Bulletin of the Earthquake Research Institute, University of Tokyo* 81: 221–232.

Gahalaut VK, Kundu B, Laishram SS, Catherine J, Kumar A, Singh MD, Tiwari R, Chadha R, Samanta S and Ambikapathy A (2013) Aseismic plate boundary in the Indo-Burmese wedge, northwest Sunda Arc. *Geology* 41: 235–238.

Gao M (ed.) (2015) *Publicizing Materials of GB 18306-2015 Chinese Ground Motion Parameter Zoning Map*. Beijing, China: China Standard Press, 264 pp (in Chinese).

Gardner JK and Knopoff L (1974) Is the sequence of earthquakes in Southern California, with aftershocks removed, Poissonian? *Bulletin of Seismological Society of America* 64: 1363–1367.

General Administration of Quality Supervision, Inspection and Quarantine of the People's Republic of China (2015) *Seismic Ground Motion Parameters Zonation Map of China (GB18306/2015)*. Beijing, China: China Standard Press.

Hanks TC and Kanamori H (1979) A moment magnitude scale. *Journal of Geophysical Research* 84: 2348–2350.

Howell BF (1985) On the effect of too small a data-base on earthquake frequency diagrams. *Bulletin of Seismological Society of America* 85: 1205–1207.

Hsu Y-J, Yu S-B, Simons M, Kuo L-C and Chen H-Y (2009) Interseismic crustal deformation in the Taiwan plate boundary zone revealed by GPS observations, seismicity, and earthquake focal mechanisms. *Tectonophysics* 479: 4–18.

Idriss IM (2014) An NGA-West2 empirical model for estimating the horizontal spectral values generated by shallow crustal earthquakes. *Earthquake Spectra* 30: 1155–1177.

Ischuk A, Bendick R, Rybin A, Molnar P, Khan SF, Kuzikov S, Mohadjer S, Saydullaev U, Ilyasova Z and Schelochkov G (2013) Kinematics of the Pamir and Hindu Kush regions from GPS geodesy. *Journal of Geophysical Research* 118: 2408–2416.

Jin J and Wang H (1988) The Qiongshan earthquake of July 1605. *Disasters* 12: 22–36.

Jin S and Park P-H (2006) Strain accumulation in South Korea inferred from GPS measurements. *Earth, Planets and Space* 58: 529–534.

Jouanne F, Awan A, Pêcher A, Kausar A, Mugnier J, Khan I, Khan N and Van Melle J (2014) Present-day deformation of northern Pakistan from Salt Ranges to Karakorum Ranges. *Journal of Geophysical Research: Solid Earth* 119: 2487–2503.

Kagan YY (1993) Statistics of characteristic earthquakes. *Bulletin of Seismological Society of America* 83: 7–24.

Kagan YY (2002a) Seismic moment distribution revisited: I. Statistical results. *Geophysical Journal International* 148: 520–541.

Kagan YY (2002b) Seismic moment distribution revisited: II. Moment conservation principle. *Geophysical Journal International* 149: 731–754.

Kagan YY, Jackson DD and Geller RJ (2012) Characteristic earthquake model, 1884-2011, R.I.P. *Seismological Research Letter* 83: 951–953.

Litchfield N, Wyss B, Christophersen A, Thomas R, Berryman K, Henshaw P and Villamor P (2013) *Guidelines for Compilation of Neotectonic Faults, Folds, and Fault Sources: GEM Faulted Earth*. Available at: www.nexus.globalquakemodel.org/gem-faulted-earth/posts/

Lü H and Zhao F (2007) Site coefficients suitable to China site category. *ACTA Seismologica Sinica* 29: 67–76.

Min Z, Wu G, Jiang Z, Liu C and Yang Y (1995) *The Catalogue of Chinese Historical Strong Earthquakes (B.C. 2300—A.D. 1911)*. Beijing, China: Seismological Publishing House, 514 pp (in Chinese).

Mohadjer S, Bendick R, Ischuk A, Kuzikov S, Kostuk A, Saydullaev U, Lodi S, Kakar DM, Wasy A, Khan MA, Molnar P, Bilham R and Zubovich AV (2010) Partitioning of India-Eurasia convergence in the Pamir-Hindu Kush from GPS measurements. *Geophysical Research Letters* 37. DOI: 10.1029/2009GL041737.

Okada Y (1992) Internal deformation due to shear and tensile faults in a half-space. *Bulletin of the Seismological Society of America* 82: 1018–1040.
Pagani M, Monelli D, Weatherill G, Danciu L, Crowley H, Silva V, Henshaw P, Butler L, Nastasi M, Panzeri L, Simionato M and Vigano D (2014) OpenQuake engine: An open hazard (and risk) software for the Global Earthquake Model. *Seismological Research Letters* 85: 692–702.
Page M and Felzer K (2015) Southern San Andreas fault seismicity is consistent with the Gutenberg–Richter magnitude-frequency distribution. *Bulletin of Seismological Society of America* 105: 2070–2080.
Petersen MD, Moschetti MP, Powers PM, Mueller CS, Haller KM, Frankel AD, Zeng Y, Rezaeian S, Harmsen SC and Boyd OS (2015) The 2014 United States national seismic hazard model. *Earthquake Spectra* 31: S1–S30.
Rong Y, Bird P and Jackson DD (2016) Earthquake potential and magnitude limits inferred from a geodetic strain-rate model for southern Europe. *Geophysical Journal International* 205: 509–522.
Rong Y, Jackson DD and Kagan YY (2003) Seismic gaps and earthquakes. *Journal of Geophysical Research* 108. DOI: 10.1029/2002JB002334.
Rong Y, Jackson DD, Magistrale H and Goldfinger C (2014) Magnitude limits of subduction zone earthquakes. *Bulletin of the Seismological Society of America* 104: 2359–2377.
Rong Y, Pagani M, Magistrale H and Weatherill G (2017) Modeling seismic hazard by integrating historical earthquake, fault, and strain rate data. In: *The proceedings of the 16th world conference on earthquake engineering*, Santiago, Chile, 9–13 January.
Rong Y, Shen Z-K, Chen G and Magistrale H (2018) *Modeling Strain Rate and Fault Slip for China and Vicinity Using GPS Data*. Washington, DC: American Geophysical Union (Abstract #T22A-01).
Schiffman C, Bali BS, Szeliga W and Bilham R (2013) Seismic slip deficit in the Kashmir Himalaya from GPS observations. *Geophysical Research Letters* 40: 5642–5645.
Schorlemmer D, Werner MJ, Marzocchi W, Jordan TH, Ogata Y, Jackson DD, Mak S, Rhoades DA, Gerstenberger MC and Hirata N (2018) The collaboratory for the study of earthquake predictability: Achievements and priorities. *Seismological Research Letters* 89: 1305–1313.
Schwartz DP and Coppersmith KJ (1984) Fault behavior and characteristic earthquakes: Examples from the Wasatch and San Andreas fault zones. *Journal of Geophysical Research* 89: 5681–5698.
Seyhan E and Stewart JP (2014) Semi-empirical nonlinear site amplification from NGA-West2 data and simulations. *Earthquake Spectra* 30: 1241–1256.
Stepp JC (1972) Analysis of completeness of earthquake sample in the Puget Sound area and its effect on statistical estimates of earthquake hazard. In: *Proceedings first Microzonation conference*, October 30–November 3, Seattle, WA, pp. 897–909.
Storchak DA, Di Giacomo D, Bondár I, Engdahl ER, Harris J, Lee WH, Villaseñor A and Bormann P (2013) Public release of the ISC-GEM global instrumental earthquake catalogue (1900–2009). *Seismological Research Letters* 84: 810–815.
Vernant P, Bilham R, Szeliga W, Drupka D, Kalita S, Bhattacharyya A, Gaur V, Pelgay P, Cattin R and Berthet T (2014) Clockwise rotation of the Brahmaputra Valley relative to India: Tectonic convergence in the eastern Himalaya, Naga Hills, and Shillong Plateau. *Journal of Geophysical Research* 119: 6558–6571.
Wang F, Wang M, Wang Y and Shen Z-K (2015) Earthquake potential of the Sichuan-Yunnan region, western China. *Journal of Asian Earth Sciences* 107: 232–243.
Wang H, Liu M, Cao J, Shen X and Zhang G (2011) Slip rates and seismic moment deficits on major active faults in mainland China. *Journal of Geophysical Research* 116. DOI: 10.1029/2010JB007821.
Wang M and Shen Z-K (2020) Present-day crustal deformation of continental China derived from GPS and its tectonic implications. *Journal of Geophysical Research* 125. DOI: 10.1029/2019JB018774.
Wang S, Wu G and Shi Z (1999) *The Catalogue of Recent Earthquakes in China* (A.D. 1912—A.D. 1990). Beijing, China: China Science and Technology Publishing House (in Chinese).
Wang W, Qiao X, Yang S and Wang D (2017) Present-day velocity field and block kinematics of Tibetan Plateau from GPS measurements. *Geophysical Journal International* 208: 1088–1102.

Wang Y, Wang E, Shen Z, Wang M, Gan W, Qiao X, Meng G, Li T, Tao W, Yang Y, Cheng J and Li P (2008) GPS-constrained inversion of present-day slip rates along major faults of the Sichuan-Yunnan region, China. *Science in China Series D: Earth Sciences* 51: 1267–1283.

Wang Y-J, Chan C-H, Lee Y-T, Ma K-F, Shyu J, Rau R-J and Cheng C-T (2016) Probabilistic seismic hazard assessments for Taiwan. *Terrestrial Atmospheric and Oceanic Sciences* 27: 325–340.

Weatherill GA, Pagani M and Garcia J (2016) Exploring earthquake databases for the creation of magnitude-homogeneous catalogues: Tools for application on a regional and global scale. *Geophysical Journal International* 206: 1652–1676.

Weichert DH (1980) Estimation of the earthquake recurrence parameters for unequal observation periods for different magnitudes. *Bulletin of Seismological Society of America* 70: 1337–1346.

Wells DL and Coppersmith KJ (1994) New empirical relationships among magnitude, rupture length, rupture width, rupture area, and surface displacement. *Bulletin of Seismological Society of America* 84: 974–1002.

Wesnousky SG (1994) The Gutenberg–Richter or characteristic earthquake distribution, which is it? *Bulletin of Seismological Society of America* 84: 1940–1959.

Wills CJ and Clahan KB (2006) Developing a map of geologically defined site-condition categories for California. *Bulletin of the Seismological Society of America* 96: 1483–1501.

Wills CJ, Gutierrez CI, Perez FG and Branum DM (2015) A next generation VS30 map for California based on geology and topography. *Bulletin of the Seismological Society of America* 105: 3083–3091.

Wills CJ, Petersen M, Bryant WA, Reichle M, Saucedo GJ, Tan S, Taylor G and Treiman J (2000) A site-conditions map for California based on geology and shear-wave velocity. *Bulletin of the Seismological Society of America* 90: S187–S208.

Woessner J, Laurentiu D, Giardini D, Crowley H, Cotton F, Grünthal G, Valensise G, Arvidsson R, Basili R and Demircioglu MB (2015) The 2013 European seismic hazard model: Key components and results. *Bulletin of Earthquake Engineering* 13: 3553–3596.

Xu X, Han Z, Yang X, Zhang S, Yu G, Zhou B, Li F, Ma B, Chen G and Ran Y (2016) *Seismotectonic Atlas of China and Its Vicinity*. Beijing, China: Earthquake Press (in Chinese).

Youngs RR and Coppersmith KJ (1985) Implications of fault slip rates and earthquake recurrence models to probabilistic seismic hazard estimates. *Bulletin of Seismological Society of America* 75: 939–964.

Yu Y, Li S and Xiao L (2013) Development of ground motion attenuation relations for the new seismic hazard map of China, *Technology for Earthquake Disaster Prevention*, 8: 24–33 (in Chinese).

Zeng Y and Shen Z-K (2014) Fault network modeling of crustal deformation in California constrained using GPS and geologic observations. *Tectonophysics* 612–613: 1–17.

Zeng Y and Shen ZK (2016) A fault-based model for crustal deformation, fault slip rates, and off-fault strain rate in California. *Bulletin of the Seismological Society of America* 106: 766–784.

Zhang P, Deng Q, Zhang G, Ma J, Gan W, Min W, Mao F and Wang Q (2003) Active tectonic blocks and strong earthquakes in the continent of China. *Science in China (Series D)* 46: 13–24.

Zhang Z, McCaffrey R and Zhang P (2013) Relative motion across the eastern Tibetan plateau: Contributions from faulting, internal strain and rotation rates. *Tectonophysics* 584: 240–256.

Zhang Z, Zhou M and Shao S (1990) *1:2,500,000 Atlas of Quaternary Geology of China and Vicinity Ocean Area*. Beijing, China: Sinamaps Press.

Zhao JX, Zhang J, Asano A, Ohno Y, Oouchi T, Takahashi T, Ogawa H, Irikura K, Thio HK and Somerville PG (2006) Attenuation relations of strong ground motion in Japan using site classification based on predominant period. *Bulletin of the Seismological Society of America* 96: 898–913.

Zubovich AV, Wang X, Scherba YG, Schelochkov GG, Reilinger R, Reigber C, Mosienko OI, Molnar P, Michajljow W, Makarov VI, Li J, Kuzikov SI, Herring TA, Hamburger MW, Hager BH, Dang Y, Bragin VD and Beisenbaev RT (2010) GPS velocity field for the Tien Shan and surrounding regions. *Tectonics* 29. DOI: 10.1029/2010TC002772.